# RSC Advances

This is an *Accepted Manuscript*, which has been through the Royal Society of Chemistry peer review process and has been accepted for publication.

*Accepted Manuscripts* are published online shortly after acceptance, before technical editing, formatting and proof reading. Using this free service, authors can make their results available to the community, in citable form, before we publish the edited article. This *Accepted Manuscript* will be replaced by the edited, formatted and paginated article as soon as this is available.

You can find more information about *Accepted Manuscripts* in the **Information for Authors**.

ROYAL SOCIETY
OF **CHEMISTRY**

www.rsc.org/advances

**A ZrN nanocrystalline coating for polymer electrolyte membrane fuel cell metallic bipolar plates prepared by reactive sputter deposition**

Jiang Xu[a,b*],　Song Xu[c],　Paul Munroe[c],　Zong-Han Xie[d,e]

a.　Department of Material Science and Engineering, Nanjing University of Aeronautics and Astronautics, 29 Yudao Street, Nanjing 210016, PR China

b.　School of Mechanical & Electrical Engineering, Wuhan Institute of Technology, 693 Xiongchu Avenue, Wuhan, 430073,P. R. China

c. School of Materials Science and Engineering, University of New South Wales, NSW 2052, Australia

d. School of Mechanical Engineering, University of Adelaide, SA 5005, Australia

e. School of Materials Science and Engineering, Tianjin Polytechnic University, Tianjin 300387, PR China

**Abstract:**

To improve the surface performance and durability of 316L stainless steel (SS) used in polymer electrolyte membrane fuel cells (PEMFCs) environments, a ZrN coating with an average grain size of ~15 nm, was deposited by reactive sputter-deposition using a double glow discharge plasma technique. The corrosion behavior of the as-deposited coating was examined and compared to uncoated 316L SS in simulated PEMFC environments (i.e., $0.5 M H_2SO_4 + 2$ ppm HF solution) by potentiodynamic and potentiostatic polarizations along with electrochemical impedance spectroscopy (EIS). The results showed that the corrosion resistance of the ZrN-coated 316L SS was significantly higher than that of uncoated material. Additionally, in comparison with uncoated 316L SS, the interfacial contact resistance (ICR) between the ZrN-coated 316L SS and the simulated gas diffusion layer (i.e., conductive carbon paper) was reduced by two orders of magnitude and remained mostly unchanged after potentiostatic polarization for 5 h. Furthermore , the average contact angle with water for the ZrN coated 316L SS (84.9°) was higher than that of uncoated material (64.4°), indicating that the ZrN-coated 316L SS is more hydrophobic.

**Keywords**: Proton exchange membrane fuel cell (PEMFC); Bipolar plate; Stainless steel; ZrN coating; Corrosion.

**1. Introduction**

1

*Corresponding authors.

E-mail addresses: xujiang73@nuaa.edu.cn (J. Xu)

Polymer electrolyte membrane fuel cells (PEMFCs) are considered to be promising power sources for transportation and portable applications, due to its high efficiency of energy conversion, low temperature operation, quick start-up time and environmentally friendly, near-zero emissions [1,2]. As one of the key components for PEMFC stacks, bipolar plates account for a significant fraction of the total price and almost all of the weight and volume of the stacks. They provide multiple important functions in PEMFC stacks, such as constituting the backbone of serially connected cells, collecting the electrical current, facilitating water and thermal management through the stack, as well as introducing the reactive gases etc [3]. An ideal bipolar plate, therefore, should have good corrosion resistance, high electrical conductivity, specific strength, chemical stability and be simple to manufacture, as well as exhibit good hydrophobicity [4,5]. Currently, graphite and graphite-based composites are widely used to fabricate these bipolar plates, but their easy permeability to reactant gases, low cost effectiveness and poor machinability, induced by their brittleness, remain major obstacles to broader commercial application. Metals are an attractive substitute for traditional graphite-based materials, since they possess good electrical conductivity, excellent manufacturability, low gas permeability and high mechanical strength. Among various metals, stainless steel (SS) has received much attention, and is considered to be the most potential alternative material for the widely used non-porous graphite in an attempt to lower the price and volumetric size of the entire fuel cell stack [6]. Unfortunately, stainless steel suffer from severe corrosive attacks when exposed to harsh acidic (pH 2-3), humid, and warm (65-90℃) working conditions typical of a PEMFC [7]. The release of metallic-based cations like $Fe^{3+}$, $Ni^{2+}$ and $Cr^{3+}$ from the dissolution of the stainless steel bipolar plates can contaminate other parts of the cell and poison the polymer membrane and catalyst layers. This leads to a significant deterioration of overall performance and reduction of service life for the PEMFC [8]. Furthermore, a passive film developed on the stainless steel surface results in increased interfacial contact resistance (ICR) between the corroded plates and the neighbouring gas diffusion layer, thereby raising the overall ohmic resistance of the cell [9]. For this reason, considerable efforts are being made employing various coatings to protect stainless steel bipolar plates from the hostile PEMFC environments [10-12]. To date, a grave challenge for these coatings prepared by various surface modification techniques is the presence of defects, such as pinholes, pores and macro-droplets, which act as corrosion channels for

localized attack by aggressive media [13]. However, our recent work has demonstrated that the double glow discharge plasma technique has the potential to engineer thick, dense coatings onto metal substrates for corrosion prevention [14-16].

Transition metal nitrides have an unusual combination of mechanical, physical and chemical properties [17]. As such, they are commonly used as protective coatings, for instance, on mechanical tools and optical devices. Among them, zirconium nitride (ZrN) has recently attracted considerable interest, notably in the area of coatings, due to its relatively low electrical resistivity and high corrosion resistance [18]. Turan et al.[19] investigated the change of contact resistance of the ZrN coated 316L SS samples before and after they were exposed to the proton exchange membrane fuel cells (PEMFC) operating conditions. The results showed that the ZrN coating had similar ICR performance before and after exposure to corrosion and improved conductivity of the 316L SS samples. Yoon et al.[20] examined the corrosion behavior of the ZrN coated 304SS samples in a simulated PEMFC environment by polarization test. They found that the ZrN coated 304SS samples satisfied the corrosion current density requirement of DOE at both anode and cathode potentials. These preliminary studies have demonstrated that ZrN could be used as coating material to extend the service life and performance of metallic bipolar plates. It is worth noting that the corrosion resistance and electrical conductivity of the ZrN coating depends predominantly on its microstructural features and corrosion product formed on its surface. However, no detailed and systematic studies have been available to date, which affect the reliability and hinder application of this promising coating material for PEMFCs.

In this work, a ZrN nanocrystalline coating was engineered onto a 316L SS substrate using a double glow discharge plasma technique. The electrochemical characteristics, interfacial contact resistance and surface wettability of the as-deposited coating were investigated and compared with uncoated 316 SS to weigh up ZrN's potential as a protective coating for PEMFC bipolar plates.

## 2. Experimental details

### 2.1. Preparation of ZrN nanocrystalline coating

The ZrN nanocrystalline coating was deposited onto 316L SS substrate using a double cathode glow discharge apparatus. In the process of double cathode glow discharge, one cathode serves as the target fabricated from the desired sputtering materials, and the other cathode as the substrate material, as described elsewhere [14]. When two different voltages are applied to the two cathodes,

glow discharge occurs. A 99.99% pure Zr disk in size of $\Phi 80 \times 4$ mm was used as the sputtering target. The substrate material was a 316L SS plate with dimensions 60mm×30mm×4mm and its nominal composition in wt.% was : Ni :11.54; Mo :2.59;Cr :16.39; C :<0.03; Si :<1.00; Mn :<2.00; P :<0.04; S :<0.03 and Fe : balance. Before sputter deposition, the polished substrates were ultrasonically cleaned in acetone, alcohol, distilled water and then dried. The working pressure was set at 35 Pa consisting of an $Ar/N_2$ gas mixture, with an $Ar:N_2$ flux ratio of 10:1. The detailed deposition parameters are as follows: target electrode bias voltage with direct current, -800 V; substrate bias voltage with impulse current, -350 V; substrate temperature, 650°C 0; target/ substrate distance, 10 mm and treatment time, 2 h.

## 2.2. Phase and microstructure characterization

The phase composition of the as-deposited coating was characterized using X-ray diffraction (XRD) (D8ADVANCE using Cu Kα radiation), with the instrument operating at 35 kV and 40 mA. X-ray data were collected using a 0.1° step scan with a count time of 1 s. The cross-sectional and corroded surface morphology of the as-deposited coatings were studied by scanning electron microscopy (SEM,Quanta200, FEI Company). Transmission electron microscopy (TEM) and high-resolution transmission electron microscopy (HRTEM) images were performed using a JEOL JEM-2010 at an accelerating voltage of 200 kV. Thin-foil specimens for TEM observation were prepared by single-jet electropolishing from the untreated side of the substrate. All X-ray photoelectron spectroscopy (XPS) measurements were performed with a Kratos AXIS Ultra ESCA System using an Al Kα X-ray source with an energy of 1486.68 eV. The accelerating voltage and emission current of the X-ray source were kept at 13 kV and 12 mA, respectively. The base pressure of the sample analysis chamber was maintained at $\sim 10^{-10}$ Torr. The pass energy was selected to be 100 eV for survey scans and 20 eV for feature scans to ensure high resolution and good sensitivity. After subtracting the background signal, the spectra were fitted by both Gaussian and mixed Gaussian/Lorentzian functions. Peak positions were then calibrated with respect to the C1s peak at 285 eV from hydrocarbon contamination. Peak identification was performed with reference to the NIST XPS database (V4.0).

## 2.3. Electrochemical measurements

Electrochemical measurements were evaluated in a 0.5 M $H_2SO_4$ + 2 ppm HF solution maintained at 70 ℃ to simulate the aggressive PEMFCs environment using a CHI660C

4

electrochemical workstation. A standard three-compartment cell was used with a working electrode, a platinum sheet as the counter electrode and a saturated calomel electrode (SCE) as the reference electrode. Throughout this paper, all electrode potentials were referred to the SCE. The potentiodynamic current–potential curves were recorded at a sweep rate of 20 mVmin$^{-1}$. Prior to and during the electrochemical measurements, the solution was purged with either hydrogen (99.99% purity) or air, to simulate the anodic or cathodic PEMFCs environments, respectively. Potentiostatic polarization measurements were carried out for 5h at −0.1 V$_{SCE}$ for the anode and +0.6 V$_{SCE}$ for the cathode environment. EIS measurement started after stabilization for about 1 h at open-circuit potential (OCP). The frequency was swept from 100 kHz down to 10 mHz, with an acquisition of 12 points per decade of frequency and an amplitude of the AC signal of 10 mV .

### 2.4. Interfacial contact resistance (ICR) and contact angle measurements

Interfacial contact resistance (ICR) values of the uncoated and ZrN coated 316L SS were determined using methods described in detail elsewhere [21].In this experimental setup, two pieces of conductive carbon paper (Toray TGP-H-090) were sandwiched between the sample and two copper plates that were plated with gold on both sides to increase conductivity. A constant electrical current of 0.5 A was applied via the two copper plates and the variation in the total voltage was recorded as a function of steadily increasing compaction force up to 260 Ncm$^{-2}$. The resistance of the carbon paper/copper plate interfaces was also measured to calibrate the ICR between the sample and carbon paper. The uncoated and ZrN coated 316L SS, after potentiostatic polarization in a simulated cathodic environment, were also investigated to understand the influence of any corrosion on ICR. The hydrophilicity of the sample surfaces was evaluated by contact angle analysis using the sessile drop method. An equal volume of distilled water was dropped carefully onto each sample by means of a micropipette. All measurements were made using a contact-angle meter (JC2000C,POWEREACH). Each measurement was repeated three times and then averaged.

### 3. Results and discussion

### 3.1. Phase identification and microstructural characterization

As shown in Fig. 1, all the X-ray diffraction peaks from the as-deposited coating can be indexed to ZrN, which exhibits a NaCl-type structure (JCPDS Card No #35-0753). In comparison with the standard powder diffraction file data for ZrN, the ZrN (200) peak is more intense,

5

indicating that the ZrN coating exhibits a strong (200) preferred orientation. From the intensity data, the preferred orientation of the as-deposited ZrN coating was evaluated in terms of texture coefficient ($TC_{hkl}$) expressed through the following equation [22]:

$$TC_{hkl} = \frac{I_m(hkl)/I_0(hkl)}{\frac{1}{n}\sum_1^n I_m(hkl)/I_0(hkl)} \tag{1}$$

where $I_m(hkl)$ is the measured X-ray relative intensity of the *(hkl)* plane, $I_0(hkl)$ is the relative intensity in the powder pattern, *(hkl)* represents the indices of the reflection plane and n is the number of reflection planes. For a $TC_{hkl}$ value greater than 1, a preferred orientation is developed towards a specific crystalline plane; while a $TC_{hkl}$ value close to 1 signifies a more random orientation and a $TC_{hkl}$ value in the range from 0 to 1 denotes a lack of grain orientation for the specific plane under consideration [23]. The calculated texture coefficients for different planes for the ZrN coating are listed in Table 1. This shows that only $TC_{200}$ is greater than unity. It is understood that, during the process of coating deposition and growth, the preferential crystallographic direction of a coating is driven by the requirement for lowering the total energy. This comprises two thermodynamic parameters, namely the free surface energy and the strain energy [24]. For B1-NaCl–structured ZrN, the (111) plane exhibits the lowest strain energy, whereas the (200) plane exhibits the lowest surface energy[25]. Several researchers have suggested that a (200) preferred orientation is associated with deposition conditions, such as high deposition temperature [26] or high $N_2$ partial pressures [27], where the surface energy factor is dominant. This observation is also consistent with the relatively high deposition temperature used in the present study.

From the cross-sectional SEM micrographs (Fig.2(a)), it can be seen that the as-deposited coating, with a thickness of ~10 μm, exhibits a homogeneous and dense structure and bonds well to the 316L SS substrate with no visible defects across the entire coating thickness. Plan-view TEM bright-field/dark-field images of the ZrN coating are shown in Fig. 2(b) and (c), together with corresponding selected area electron diffraction (SAED) pattern. Clearly, the coating is composed of equiaxed grains with an average grain size of ~15 nm, and the selected area diffraction rings (inset in Fig. 2(c)) from inside to outside, respectively, correspond to the (111), (200), (220) and (311) planes of B1-NaCl–structured ZrN. An intense ZrN (200) ring in the SAED pattern provides further evidence that the coating exhibits a strong ZrN (200)-oriented texture, in

agreement with the XRD data. A bright-field HRTEM lattice image (Fig. 2(d)) shows that the spacing of the lattice fringes are determined to be 2.28 and 2.66 Å, which correspond to the (200) and (111) lattice planes of B1-NaCl–structured ZrN, respectively.

### 3.2. Electrochemical corrosion

### 3.2.1. Potentiodynamic polarization studies

Fig. 3(a) and (b) presents the potentiodynamic polarization curves for uncoated and ZrN-coated 316L SS in simulated anodic and cathodic PEMFC environments. Before each measurement the specimens were polarised cathodically for 10 min to provide reproducible initial conditions of the specimens surface. The corrosion potential ($E_{corr}$), corrosion current density ($i_{corr}$), and anodic ($\beta_a$) and cathodic ($\beta_c$) Tafel slopes were derived from the polarization curves using Tafel analysis and are summarized in Table 2. Moreover, current density at the operating potential in both the anodic and cathodic environments is also listed in Table 2. As shown in Fig. 3(a) and (b), a small peak from the active–passive transition is present on the anodic branch of the polarization curves for the uncoated 316L SS, while the ZrN-coated 316L SS exhibits a nature of passivation behavior without the presence of any active/passive transient peak. In both cases, the uncoated 316L SS has a negative corrosion potential ($E_{corr}$) of about –0.25 $V_{SCE}$, while the ZrN coating has a more positive $E_{corr}$, implying the higher chemical inertness and stability of the ZrN coating. The corrosion current density ($i_{corr}$) of the ZrN-coated 316L SS is more than two orders of magnitude lower than that of the uncoated 316L SS when both purged with air and $H_2$, suggesting that the corrosion rate of 316L SS is reduced by the application of the ZrN nanocrystalline coating. At potential above +0.5 $V_{SCE}$ , the current density of the bare 316L SS continuously increases with potential, characterized by the occurrence of transpassivation, but the ZrN-coated 316L SS exhibits a wide passive plateau extended up to +1.0 $V_{SCE}$ without any pitting corrosion. Furthermore, the current density of the uncoated 316L SS at the anodic operating potential of −0.1 $V_{SCE}$ is 11.2 µA ·cm$^{-2}$, whereas that of the ZrN-coated 316L SS under the same condition is 0.847µA ·cm$^{-2}$, revealing that the ZrN coating provides cathodic protection for the stainless steel substrate. At the typical PEMFC cathodic operation potential of +0.6 $V_{SCE}$, the 316L SS is in the trans-passive region with the corrosion current density of $6.24\times10^3$ µA·cm$^{-2}$, whereas the ZrN coating is in the passive region and its corrosion current is $7.43\times10^{-1}$ µA·cm$^{-2}$. Such a low value meets the U.S.Department of Energy (DoE) electrochemical corrosion target of 1µA·cm$^{-2}$[28].

### 3.2.2. Potentiostatic polarization measurements and XPS analysis

Under actual PEMFC operating conditions, the bipolar plates undergo corrosion at different applied potentials (anode environment: –0.1 $V_{SCE}$ ; cathode environment: +0.6 $V_{SCE}$ ). In view of this, the potentiostatic polarization tests were also employed to evaluate the corrosion resistance of specimens at anode and cathode potentials in a simulated PEMFC solution. Fig. 4(a) and (b) show the current density as a function of exposure time for the uncoated and ZrN-coated 316L SS in 0.5 M $H_2SO_4$ + 2 ppm HF solution at the anode (–0.1 $V_{SCE}$ purged with $H_2$) and cathode (+0.6 $V_{SCE}$ purged with air) potentials, respectively. As shown in Fig.4(a), in the simulated anodic environment, the current density of the uncoated 316L SS drops rapidly over the first 1000 s, then slowly increases, and finally reaches a stable value of 3.59 $\mu A \cdot cm^{-2}$. By comparison, the ZrN-coated 316L SS always exhibits a negative current density of about -1.51 $\mu A \cdot cm^{-2}$ over the entire test duration, since the simulated anode potential is cathodic to the ZrN coated 316L SS. The negative current density can mitigate the active dissolution rate of the ZrN coated 316L SS induced by cathodic protection. As shown in Fig.4(b), at the cathode potential, the current density recorded from the uncoated 316L SS first decreases rapidly initially and then gradually stabilizes at about 4.58 $\mu A \cdot cm^{-2}$. This is one order of magnitude higher than that of the ZrN coated specimen. Furthermore, obvious fluctuations of current density appear in the two potentiostatic curves for the uncoated 316L SS. These fluctuations of the recorded current density are attributed to the initiation and repassivation of metastable pits, signifying that the protective film formed on the uncoated 316L SS is unstable in both simulated anodic and cathodic PEMFC environments. Similarly, strong fluctuations of current density for TiN coatings prepared by physical vapor deposition (PVD) tested in aggressive PEMFC conditions have been reported elsewhere [29,30].This fluctuation arises mainly from the presence of defects in these coatings such as pin-holes and micro porosity. These structural defects act as inward diffusion paths for corrosive species into the substrate, which promote galvanic corrosion between the coating and substrate. Hence, compared with TiN coatings prepared by PVD, the ZrN coating fabricated in this study by a double glow discharge plasma technique exhibits a more dense structure, which can more effectively hinder corrosive species from entering the substrate. To better understand the difference in the corrosion resistance between the uncoated and ZrN coated 316L SS, the surface morphologies of two specimens after the potentiostatic polarization in the simulated cathodic

8

(+0.6 $V_{SCE}$ purged with air) environments were examined by SEM and shown in Fig. 5. It is obvious that some pits with hundreds of micrometer in length are distributed on the surface of the uncoated 316L SS, whereas no visible corrosion trace is apparent on the surface of the ZrN coated 316L SS. This is in accordance with the results of potentiodynamic polarization tests, because at cathode potentials, the 316L SS and ZrN coating are in the transpassive region and passive region, respectively.

Fig.6 shows high-resolution XPS spectra for the Zr 3d and N1s of the ZrN coating before and after potentiostatic polarization in simulated cathodic environment (at +0.6 $V_{SCE}$ purged with air for 5 h). As shown in Fig.6(a), the Zr 3d spectrum exhibits a doublet with Zr $3d_{5/2}$ and Zr $3d_{3/2}$ peaks at 179.9 and 182.3 eV, respectively, corresponding to the Zr–N bond in stoichiometric ZrN[31]. Similarly, the N 1s spectrum shows a single peak at a binding energy of 397.4 eV, which is assigned to the chemical state of N in stoichiometric ZrN[32]. According to the XPS results, no significant changes were observed for the chemical bonding states of ZrN-coated 316L SS after potentiostatic polarization, implying that the ZrN coating exhibits good electrochemical stability in PEMFC environment without the presence of any corrosion products (or oxide films) on the coating surface.

### 3.2.3. Electrochemical impedance measurements (EIS)

Electrochemical impedance spectroscopy (EIS) has been broadly used for characterization of corrosion resistance of coated systems in aqueous corrosive environments [33,34]. This method provides information about the coating quality, such as defects, adhesion, barrier properties, as well as the destruction of the protective system metal/coating [35]. Fig. 7(a) and (b) show the representative Nyquist and Bode plots of the uncoated and ZrN-coated 316L SS at respective open circuit potentials in 0.5 M $H_2SO_4$ + 2 ppm HF solution at 70℃, respectively. It is clear that the Nyquistplot for the uncoated 316L SS only displays a depressed capacitive semicircle over the entire frequency range, and the corresponding Bode plot shows high symmetry with a maximum phase angle closely approaching −72∘. The one time constant equivalent circuit $R_s(R_pQ_p)$ (i.e., modified Randles circuit) shown in Fig. 8(a) was applied to simulate the experimental impedance data. This equivalent circuit consists of an electrolyte resistance (Rs) in series with the parallel combination of a constant phase angle element (CPE, $Q_p$) and a resistance $R_p$ (polarization resistance). The physical significance of the elements of the Randles circuit has been widely

reported in the literature [36], where $R_s$ represents the solution resistance, and $Q_p$ and $R_p$ are the constant phase element and polarization resistance, respectively. During the fitting of the impedance spectra, a constant-phase element (CPE) was used instead of a pure capacitance to obtain a satisfactory impedance simulation, due to surface heterogeneities originating from surface roughness, porosity or inhomogeneous distribution of the electrode surface properties [37]. The impedance function of the CPE is represented by :

$$Z_{CPE} = \frac{1}{Y_0(j\omega)^n} \tag{2}$$

where $Y_0$ is the admittance magnitude of CPE, $j$ is the imaginary unit and $\omega$ is the angular frequency. The factor $n$, defined as a CPE exponent, is an adjustable parameter that always has a value between 0.5 and 1. When n = 1, the CPE represents an ideal capacitance; for 0.5 < n < 1, the CPE describes a distribution of dielectric relaxation times in frequency space; and when n = 0.5, the CPE represents a Warburg impedance with diffusional character. Moreover, the time constant ($\tau$), expressed as $\tau = C \times R$, can be used to describe the rate of the relevant electrochemical process [38]. Table 3 compiles the numerical values of circuit elements from the fitting procedure. The chi-square($\chi^2$) value of $2.49\times10^{-3}$ shows a good agreement between the equivalent circuit predictions and the experimental data, suggesting that this equivalent circuit model reasonably reflects the electrochemical process occurring in the 316L SS /passive film/electrolyte system.

From the Bode plot in Fig.7 a, the ZrN-coated 316L SS shows significantly larger capacitive loops than the uncoated 316L SS. From the corresponding Bode plot (Fig.7 b), it is evident that the log |Z| increases linearly with decreasing frequency (log $f$ ), with a slope close to -1 at the middle and low frequency range in the Bode-magnitude plots and a broad plateau with a phase angle near −80◦ that is independent of the frequency maximum observed in the Bode-phase plots. These features are characteristic response of a near-capacitive behavior, which is typical of passive systems [39]. Therefore, the electrochemical impedance spectra for the ZrN-coated 316L SS just reveal the impedance responses from the ZrN coating due to the absence of pin-hole defects. The ZrN-coated 316L SS shows much larger diameter of capacitive loop, wider frequency regions with phase angle near −90◦ and higher low frequency limit ($|Z|_{f\rightarrow0}$) than the uncoated 316L SS, suggesting that the application of the ZrN coating has greatly improved the corrosion resistance of 316L SS in the simulated PEMFC solution. This is in agreement with the results obtained from the

potentiodynamic and potentiostatic polarization measurements. An equivalent circuit, as shown in Fig.8(b), was set up to interpret the impedance data obtained from the ZrN-coated 316L SS. Here, $R_s$ is the resistance of the solution, $R_{ct}$ is charge-transfer resistance, $C_{coat}$ is the capacitance of the ZrN coating, $R_{film}$ is the resistance to ion diffusion in the ZrN coating, and the constant phase element (CPE) is related to the double-layer capacitor. It is apparent from Fig.7 that good agreement is obtained between the measured and the fitted spectra at high and low frequencies, suggesting the validity of the proposed circuit model. As can be seen from Table 3, the values of $R_{film}$ and$\tau_2$ are significantly larger than that of $R_{ct}$ and $\tau_1$, revealing that the resistance to ion diffusion in the ZrN coating is predominantly responsible for anticorrosive protection of the coated 316L SS. The resistance value, $R_{film}$ of the ZrN-coated 316L SS is rather large and are of the order of $10^7 \Omega$ cm$^2$, which is two orders of magnitude higher than that of the uncoated 316L SS. Moreover, the time constant ($\tau$) for the ZrN-coated 316L SS is also obviously larger than that of the bare 316L SS. The results show that the ZrN coating behaves as an efficient barrier to corrosion, and has an obvious retarding effect on the electrochemical corrosion process.

### 3.3. Interfacial contact resistance

A reduction in interfacial contact resistance (ICR) between the bipolar plate and the gas diffusion layer (GDL) is beneficial for minimizing any loss of power obtained from the PEMFC stack [41]. Candidate materials for these plates should offer good corrosion resistance along with low interfacial contact resistance. The ICR values for the bare and ZrN-coated 316L SS before and after exposure to potentiostatic polarization in 0.5 M $H_2SO_4$ + 2 ppm HF solution at cathode (+0.6 $V_{SCE}$ purged with air) and anode (–0.1 $V_{SCE}$ purged with $H_2$) potentials for 5 h are plotted as a function of compaction force in Fig.9. All of the measured contact resistance between the interface of tested samples and simulated GDL of Toray TGP-H-060 carbon paper as a function of compaction pressures follow a similar trend, where the ICR values decrease with increasing compaction force and eventually reach a stable value as the compaction force is increased to a certain value. In general, the decrease in the ICR value with increasing compaction force is attributed to an increase in the effective contact area between samples and carbon paper, and above a certain value of compaction force, the effective contact area does not increase any further, hence the ICR value becomes constant. At a compaction force of 140 N cm$^{-2}$, a typical compaction force applied to the stack, the ICR value between the uncoated 316L SS and the carbon papers is

11

159.7 m$\Omega \cdot$cm$^{-2}$, which is broadly consistent with other reported results which are of the order of 100-160 m$\Omega \cdot$cm$^{-2}$ under the same compaction force. After 5 h potentiostatic polarization at +0.6 V$_{SCE}$ purging with air and at –0.1 V$_{SCE}$ purged with H$_2$, the ICR values for the uncoated 316L SS increase to 265.3 and 238.5 m$\Omega \cdot$cm$^{-2}$, respectively. The high contact resistance of the uncoated 316L SS mainly arises from the air-formed oxide film on the steel surface and this oxide layer becomes thicker under a high cathode potential in an oxidizing atmosphere, leading to higher ICR value. However, After 5 h potentiostatic polarization at +0.6 V$_{SCE}$ purging with air and at –0.1 V$_{SCE}$ purged with H$_2$, the ICR values for the ZrN-coated 316L SS increase from 7.4 m$\Omega \cdot$cm$^{-2}$ to 9.2 and 8.5 m$\Omega \cdot$cm$^{-2}$. Both of these values are lower than the DOE's 2020 technical target of 10 m$\Omega \cdot$cm$^{-2}$. The lower ICR value for the ZrN coating is inextricably related to its band structure. Band-structure calculations show that for ZrN, with a NaCl structure, the Fermi energy (E$_F$) lies in the "d band" and is primarily derived from Zr 4d states with a relatively high density of states (DOS)[42]. As a result, ZrN exhibits metallic electrical conductivity with a bulk resistivity of around 20 $\mu\Omega$ cm [43]; a value lower than that for pure Zr (42 $\mu\Omega$ cm).

### 3.4. Contact angle

   The presence of water in a PEMFC stack originates either from an oxygen reduction reaction at the catalyst cathode or is fed externally into the cell through humidification or the presence of cooling gases [44]. Moreover, excess water can not only block the reaction sites of neighbouring electrodes, preventing the access of reactant gases to the cell, but also accelerate the rate of corrosion of the metallic bipolar plates [45]. To avoid issues associated with flooding and power degradation due to the submergence of the catalyst, the surface wettability of the bipolar plate materials should be sufficiently low enough to immediately remove any redundant water from PEMFC stack. Contact angle measurements provide a means to estimate the wettability of a surface [46]. A high contact angle denotes a low surface wettability. Figs. 10 (a) and (b) shows photographs of water droplets on the uncoated and ZrN-coated 316L SS, respectively. The average contact angle with water for the ZrN-coated 316L SS is 84.9°, while for the uncoated 316L SS it is 64.4°. These results imply that the ZrN-coated 316L SS is more hydrophobic than the uncoated 316L SS. This coated surface therefore provides greater protection from accumulated water flooding the electrode system [47]. Furthermore, a lower wettability also means a lower fraction of the coated area is in contact with the electrolyte solution, thus lowering the extent of any corrosion

that may occur.

## 4. Conclusions

A nanocrystalline ZrN coating was prepared by a double glow discharge plasma technique on the 316L stainless steel substrate used for fuel cell bipolar plates. The as-deposited coating exhibited a homogeneous and dense structure that consisted of equiaxed grains with an average size of ~15 nm. The electrochemical behaviour of the coating was characterised in simulated PEMFC environments using potentiodynamic and potentiostatic polarizations as well as electrochemical impedance spectroscopy (EIS). The corrosion resistance of the ZrN-coated 316L SS was significantly improved in comparison with that of uncoated 316 SS. Under a compaction force of 140 N cm$^{-2}$, the ICR values for the ZrN coated 316L SS was reduced by two orders of magnitude and meets the requirement made by the U.S. DoE (10 mΩ·cm$^{-2}$) with a negligible change before and after potentiostatic polarization tests. Moreover, the ZrN-coated 316L SS is more hydrophobic than the uncoated steel, which prevents accumulated water from flooding the electrode system and lowers the extent of corrosive attack. The unique combination of high corrosion resistance, good electrical conductivity and low surface wettability therefore renders the nanocrystalline ZrN coating an attractive choice for enhancing the surface performance and durability of bipolar plates in PEMFCs.

**Reference**

[1]   P. Ekdunge, M. Råberg, Int. J. Hydrog. Energy 23 (1998) 381-385.

[2]   J. Hackney, R. De. Neufville, Transp. Res. Pt. A-Policy Pract. 35 (2001) 243-266.

[3]   H. Tawfik, Y. Hung, D. Mahajan, J. Power Sources 163 (2007) 755-767.

[4]   V. V. Nikam, R. G. Reddy, J. Power Sources 152 (2005) 146-155.

[5]   V. V. Nikam, R. G. Reddy, Electrochim. Acta 51 (2006) 6338-6345.

[6]   K. H. Cho, W. G. Lee, S. B. Lee, H. Jang, J. Power Sources 178 (2008) 671-676.

[7]   K. H. Hou, C. H. Lin, M. D. Ger, S. W. Shiah, H. M. Chou, Int. J. Hydrog. Energy 37 (2012)

3890-3896.

[8]   H. Wang, J. A. Turner, Fuel Cells 10 (2010) 510-519.

[9]   H. Wang, M. A. Sweikart, J. A. Turner, J. Power Sources 115 (2003) 243-251.

[10] C. Y. Chung, S. K. Chen, P. J. Chiu, M. H. Chang, T. T. Hung, T. H. Ko, J. Power Sources

176 (2008) 276-281.

[11] A. Pozio, F. Zaza, A. Masci, R. F. Silva, J Power Sources 179 (2008) 631-639.

[12] D. G. Nam, H. C. Lee, J Power Sources 170 (2007) 268-274.

[13] J. Barranco, F. Barreras, A. Lozano, M. Maza, J. Power Sources 196 (2011) 4283-4289.

[14] C. Zhou, J. Xu, S. Jiang, Mater. Charact. 61 (2010) 249 -256.

[15] J. Xu, D. Lai, Z. Xie, P. Munroe, Z. T. Jiang, J. Mater. Chem. 22 (2012) 2596-2606.

[16] J. Xu, L. Liu, Z. Li, P. Munroe, Z. H. Xie, Acta Mater. 63 (2014) 245-260.

[17] C. Stampfl, W. Mannstadt, R. Asahi, A. J. Freeman, Phys. Rev. B 63 (2001) 106-155.

[18] H. M. Benia, M. Guemmaz, G. Schmerber, A. Mosser, J. C. Parlebas, Appl. Surf. Sci. 200

(2002) 231-238.

[19] C.Turan, Ö.N.Cora, M.Koc, Int. J. Hydrog. Energy, 37 (2012) 18187-18204

[20] W.Yoon, X.Huang, P.Fazzino, K.L. Reifsnider, M.A. Akkaoui, J. Power Sources 179 (2008)

265–273

[21] H. Wang, M. A. Sweikart, J. A. Turner, J. Power Sources 115 (2003) 243-251.

[22] M. I. Jones, I. R. McColl, D. M. Gran, Surf. Coat. Technol. 132 (2000) 143-151.

[23] C. Y. Su, C. T. Lu, W. T. Hsiao, W. H. Liu, Thin Solid Films 544 (2013) 170-174.

[24] K. Ashok, B. Subramanian, P. Kuppusami, M. Jayachandran, Cryst. Res. Technol. 44 (2009)

511-516.

[25] D. E. Wolfe, J. Singh, K. Narasimhan, Surf. Coat. Technol. 160 (2002) 206-218.

[26] H. Jiménez, E. Restrepo, A. Devia, Surf. Coat. Technol. 201 (2006) 1594-1601.

[27] J. V. Ramana, S. Kumar, C. David, A. K. Ray, V. S. Raju, Mater. Lett. 43 (2000) 73-76.

[28]R. A. Antunes, M. C. L. Oliveira, G. Ett, V. Ett, Int. J. Hydrogen Energy 35 (2010) 3632-3647.

[29]M. Li, S. Luo, C. Zeng, J. Shen, H. Lin, C. Cao, Corros. Sci. 46 (2004) 1369-1380.

[30]Y. Wang, D. O. Northwood, J. Power Sources 165 (2007) 293-298.

[31]D. F. Arias, Y. C. Arango, A. Devia, Appl. Surf. Sci. 253 (2006) 1683-1690.

[32]S. Badrinarayanan, S. Sinha, A. B. Mandale, J. Electron. Spectrosc. Relat. Phenom. 49 (1989) 303-309.

[33]L. Li, E. Niu, G. Lv, X. Zhang, H. Chen, S. Fan, C. Liu, S. Z. Yang, Appl. Surf. Sci. 253 (2007) 6811-6816.

[34]B. Díaz, E. Härkönen, J. Światowska, V. Maurice, A. Seyeux, P. Marcus, M. Ritala, Corros. Sci. 53 (2011) 2168-2175.

[35]P. K. Potucek, R. G. Rateick, V. I. Birss, J. Electrochem. Soc. 153 (2006) B304- B310.

[36] H. Zohdi, H.R. Shahverdi, S.M.M. Hadavi, Electrochem. Commun. 13(2011)840-843.

[37] J. B. Jorcin, M. E. Orazem, N. Pébère, B. Tribollet, Electrochim. Acta 51 (2006) 1473-1479.

[38] A. Petrossians, J. J. Whalen, J. D. Weiland, F. Mansfeld, J. Electrochem. Soc. 158 (2011) D269-D276.

[39] A. M. Fekry, R. M. El-Sherif, Electrochim. Acta 54 (2009) 7280-7285.

[40] H. Krawiec, V. Vignal, E. Schwarzenboeck, J. Banas, Electrochim. Acta 104 (2013) 400-406.

[41]L. Zhang, Y. Liu, H. Song, S. Wang, Y. Zhou, S. J. Hu, J. Power Sources 162 (2006) 1165-1171.

[42]K. Schwarz, A. R. Williams, J. J. Cuomo, J. H. E. Harper, H. T. G. Hentzell, Phys. Rev. B 32 (1985) 8312-8316.

[43]J. Westlinder, J. MalmstrÖm, G. SjÖblom, J. Olsson, Solid-State Electron. 49 (2005) 1410-1413.

[44]T. Ous, C. Arcoumanis, J. Power Sources 240 (2013) 558-582.

[45]L. Wang, J. Sun, P. Li, B. Jing, S. Li, Z. Wen, S. Ji, J. Power Sources 208 (2012) 397-403.

[46]Y. G. Takei, T. Aoki, K. Sanui, N. Ogata, Y. Sakurai, T. Okano, Macromolecules 27 (1994) 6163-6166.

[47]H. Tawfik, Y. Hung, D. Mahajan. J Power Sources 163 (2007) 755-767.
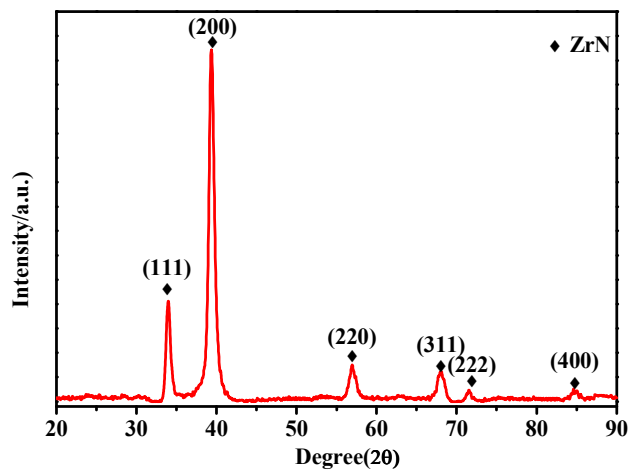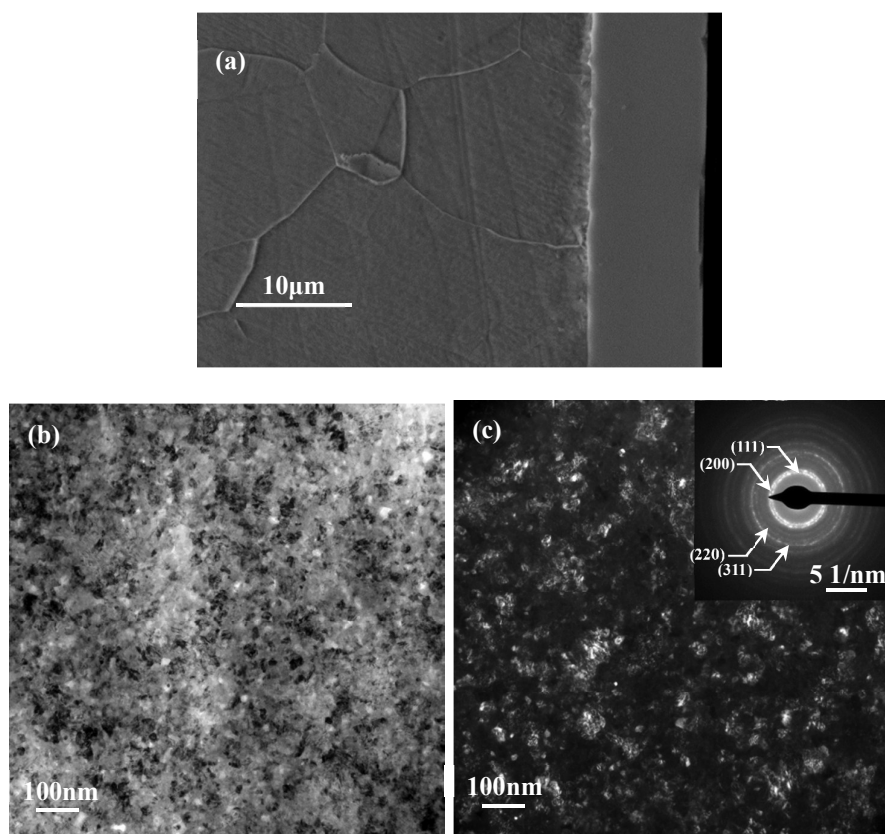
**Figure and Table captions**

**Fig.1.** Typical X-ray diffraction pattern taken from the as-deposited ZrN coating.

**Fig.2.** (a) SEM cross-sectional image of the ZrN coating; Plan-view TEM bright-field (b) /dark-field (c) images of the ZrN coating ; (d) An HRTEM image of the ZrN coating.

**Fig.3.**Potentiodynamic polarization curves of the bare and ZrN-coated 316L SS in 0.5 M $H_2SO_4$ + 2 ppm HF solution at 70 $^\circ$C purged with $H_2$ (a) and air (b).

**Fig.4.** Potentiostatic polarization curves of the bare and ZrN-coated 316L SS in 0.5 M $H_2SO_4$ + 2 ppm HF solution at anode (-0.1 $V_{SCE}$ purged with $H_2$) (a) and cathode (+0.6 $V_{SCE}$ purged with air) potentials (b).

**Fig.5.** SEM micrographs of the surface morphologies of two specimens after the potentiostatic polarization in the simulated cathodic environment (purged with air): ZrN coated (a) and uncoated 316L SS (b).

**Fig.6.**XPS spectra of (a) Zr 3d, (b) N 1s of the ZrN coating before and after potentiostatic polarization in simulated cathodic environment (at +0.6 VSCE purged with air for 5 h).

**Fig.7.** (a) Nyquist and (b) Bode plots of the bare and ZrN-coated 316L SS at respective open circuit potentials in 0.5 M $H_2SO_4$ + 2 ppm HF solution.

**Fig.8.**Equivalent electrical circuits used for modeling experimental EIS data of the bare and ZrN-coated 316L SS.

**Fig.9.** Interfacial contact resistance values of the bare and ZrN-coated 316L SS as a function of compaction force before (a) and after exposure to potentiostatic polarization in 0.5 M $H_2SO_4$ + 2 ppm HF solution at (b) cathode (+0.6 $V_{SCE}$ purged with air) and ( c) anode (-0.1 $V_{SCE}$ purged with $H_2$) potentials for 5 h.

**Fig.10.** The photographs of water droplet on the bare(a) and ZrN-coated 316L SS (b)with water.

**Table 1**     The calculated texture coefficients of different planes for the ZrN coating.

**Table 2**   Electrochemical parameters for the bare and ZrN-coated 316L SS from polarization curves: corrosion potential ($E_{corr}$) and corrosion current density ($i_{corr}$) at $E_{corr}$.

**Table 3** Electrochemical parameters obtained from equivalent circuits simulation.

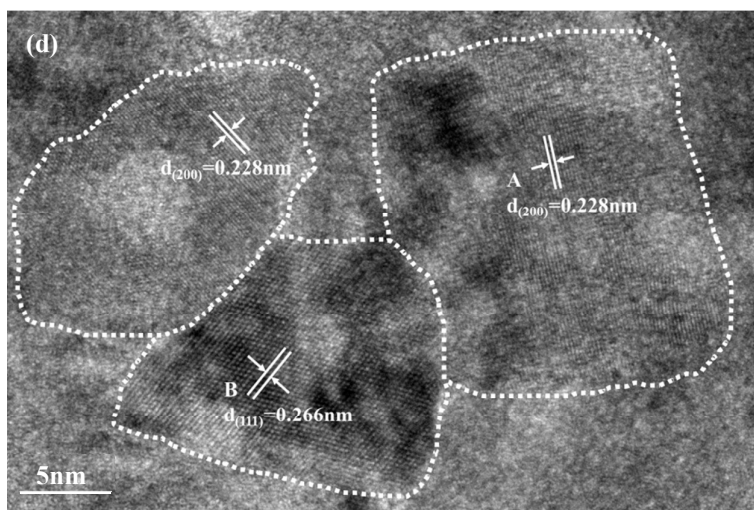Fig.1. Typical X-ray diffraction pattern taken from the as-deposited ZrN coating.

Fig.2. (a) SEM cross-sectional image of the ZrN coating; Plan-view TEM bright-field (b) /dark-field (c) images of the ZrN coating ; (d) An HRTEM image of the ZrN coating.
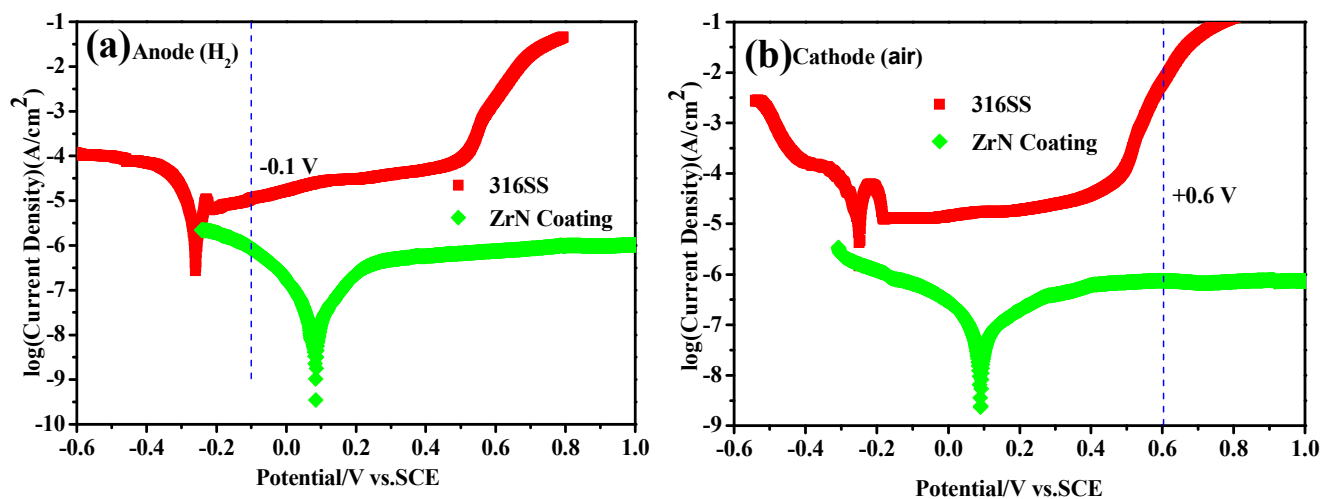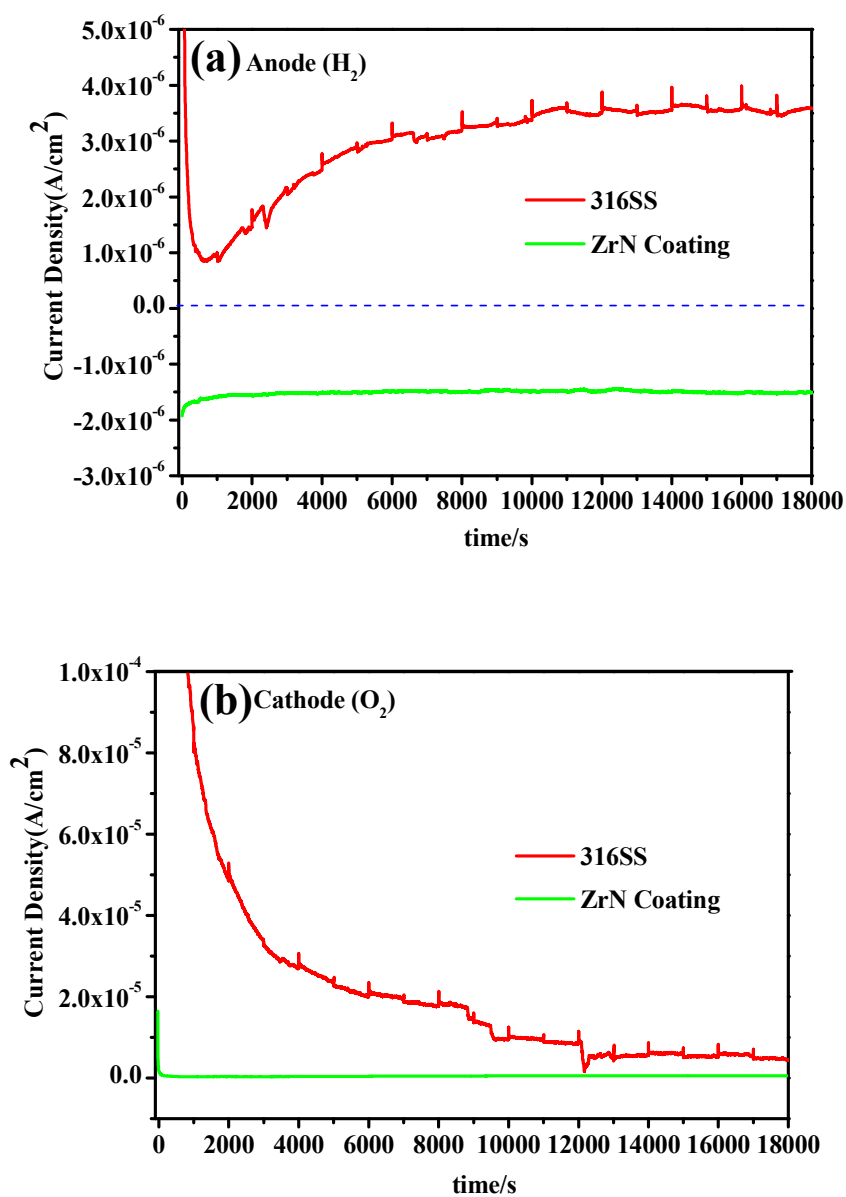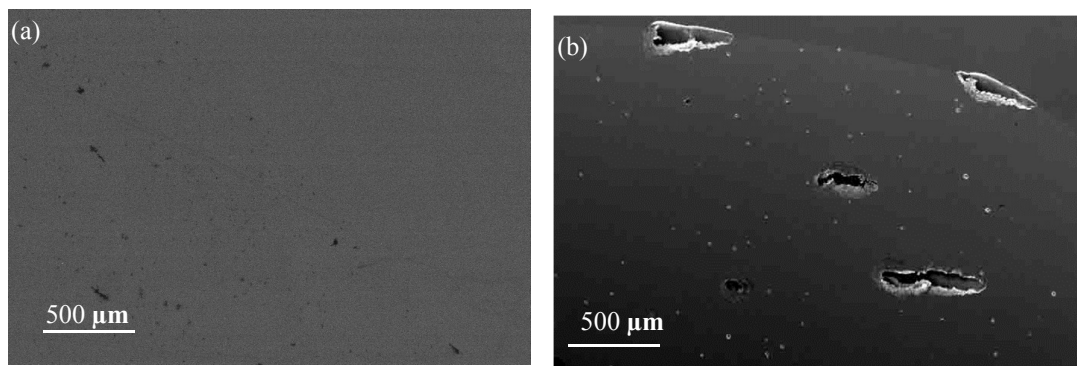


Fig.3.Potentiodynamic polarization curves of the bare and ZrN-coated 316L SS in 0.5 M $H_2SO_4$ + 2 ppm HF solution at 70 $^\circ$C purged with $H_2$ (a) and air (b).

Fig.4. Potentiostatic polarization curves of the bare and ZrN-coated 316L SS in 0.5 M $H_2SO_4$ + 2 ppm HF solution at anode (-0.1 $V_{SCE}$ purged with $H_2$) (a) and cathode (+0.6 $V_{SCE}$ purged with air) potentials (b).

Fig.5. SEM micrographs of the surface morphologies of two specimens after the potentiostatic polarization in the simulated cathodic environment (purged with air): ZrN coated (a) and uncoated 316L SS (b).
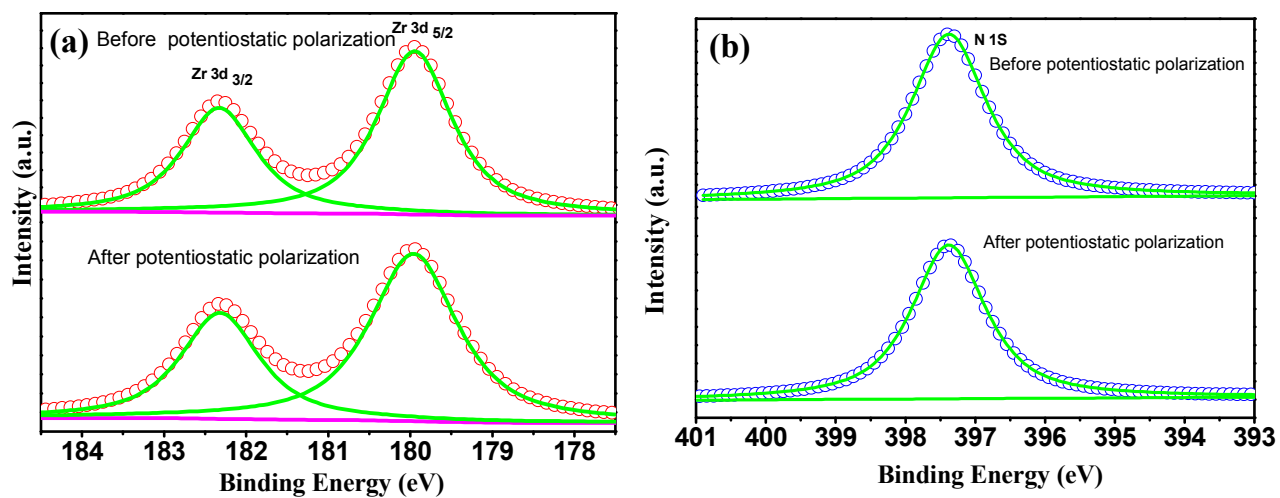


Fig.6. XPS spectra of (a) Zr 3d, (b) N 1s of the ZrN coating before and after potentiostatic polarization in simulated cathodic environment (at +0.6 VSCE purged with air for 5 h).
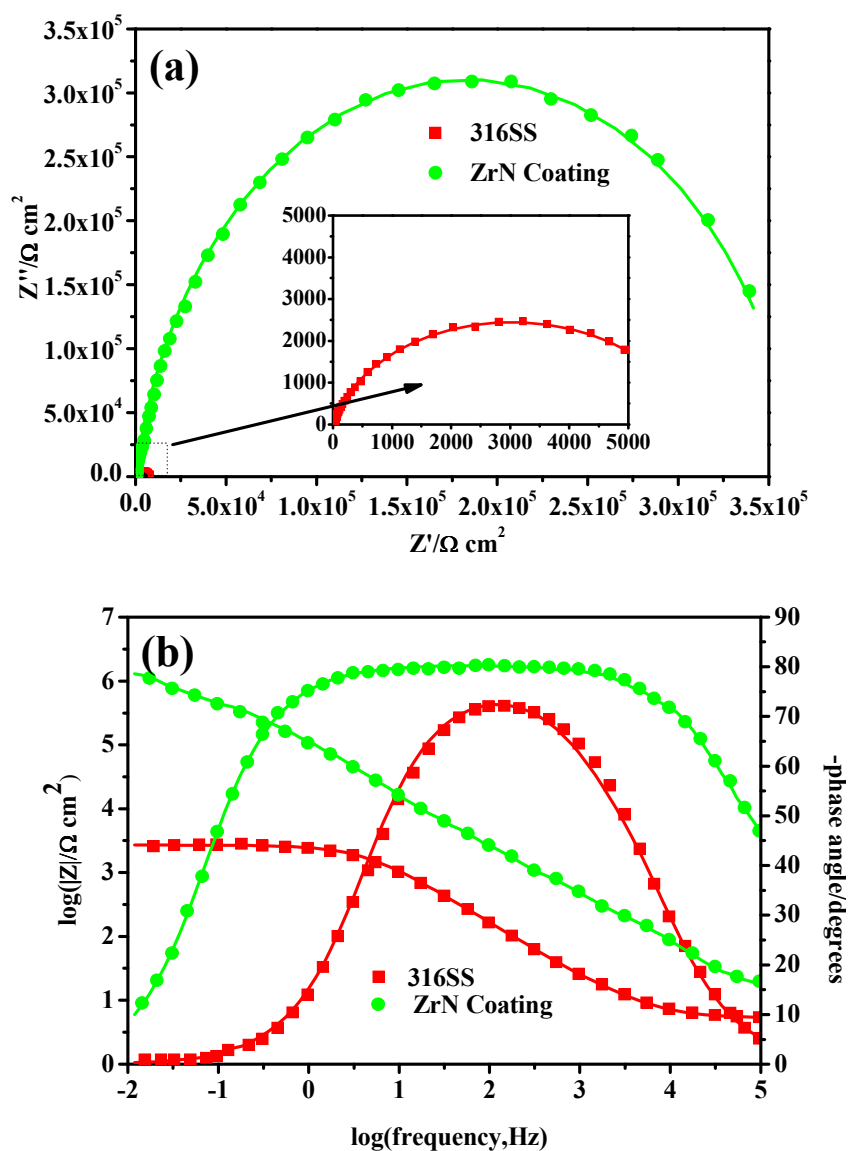
Fig.7. (a) Nyquist and (b) Bode plots of the bare and ZrN-coated 316L SS at respective open circuit potentials in 0.5 M $H_2SO_4$ + 2 ppm HF solution.
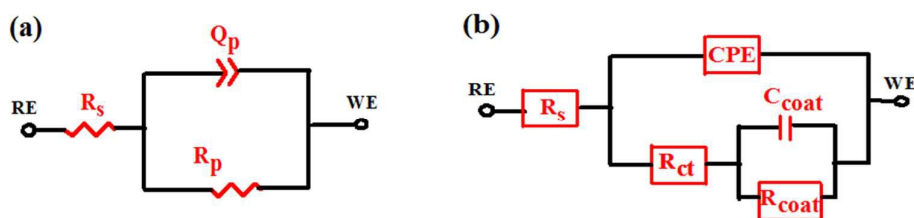


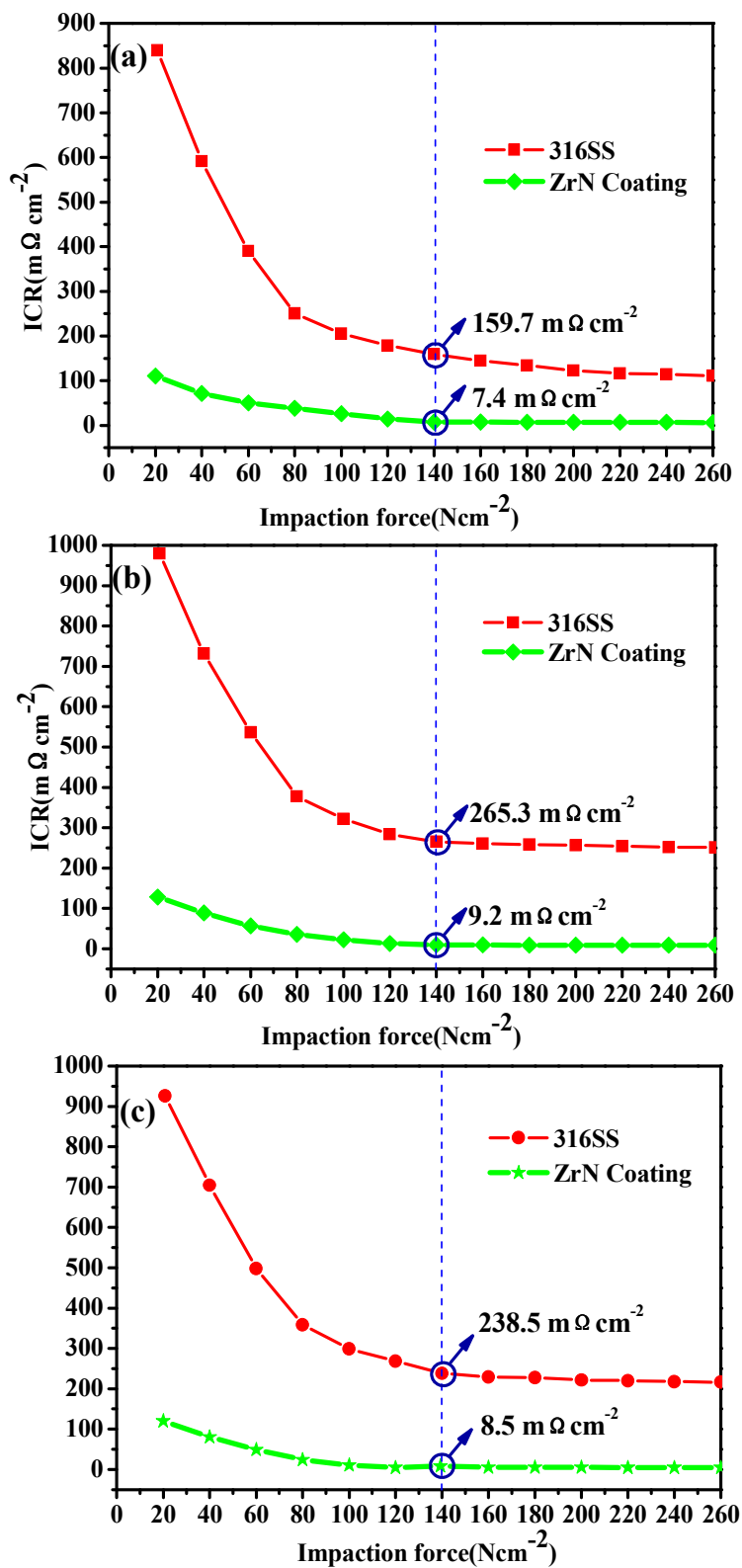Fig.8.Equivalent electrical circuits used for modeling experimental EIS data of the bare and ZrN-coated 316L SS.

Fig.9.Interfacial contact resistance values of the bare and ZrN-coated 316L SS as a function of compaction force before (a) and after exposure to potentiostatic polarization in 0.5 M $H_2SO_4$ + 2 ppm HF solution at (b) cathode (+0.6 $V_{SCE}$ purged with air) and ( c) anode (-0.1 $V_{SCE}$ purged with $H_2$) potentials for 5 h.
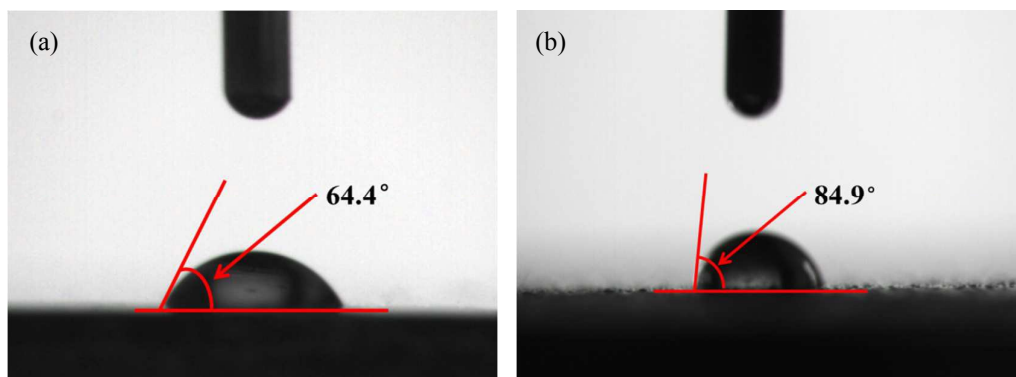
Fig.10. The photographs of water droplet on the bare(a) and ZrN-coated 316L SS (b)with water.

Table 1    The calculated texture coefficients of different planes for the ZrN coating.

| crystal plane | (111) | (200) | (220) | (311) | (222) | (400) |
|---|---|---|---|---|---|---|
| T(hkl) | 0.96 | 3.38 | 0.44 | 0.41 | 0.27 | 0.52 |

Table 2    Electrochemical parameters for the bare and ZrN-coated 316L SS from polarization curves.

| Parameters | 316SS | | ZrN | |
|---|---|---|---|---|
| | Anode | Cathode | Anode | Cathode |
| $E_{corr}$(V $_{SCE}$) | -0.26 | -0.25 | 0.08 | 0.09 |
| $i_{corr}$($\mu$A cm$^{-2}$) | 8.09 | 39.2 | $8.11\times10^{-2}$ | $1.42\times10^{-1}$ |
| $\beta_a$(V/decade) | 233.85 | 196.75 | 219.30 | 217.82 |
| $-\beta_c$(V/decade) | 113.24 | 105.34 | 195.37 | 192.53 |
| -0.1 $V_{SCE}$ ($\mu$A $\cdot$cm$^{-2}$) | 11.2 | | $-8.47\times10^{-1}$ | |
| +0.6 $V_{SCE}$ ($\mu$A$\cdot$ cm$^{-2}$) | $6.24\times10^{3}$ | | $7.43\times10^{-1}$ | |

Table 3 Electrochemical parameters obtained from equivalent circuits simulation.

| Samples | $R_s/\Omega\cdot cm^2$ | $CPE/\Omega^{-1}\cdot S^n\cdot cm^{-2}$ | $n_1$ | $C_{pf}/\mu F\cdot cm^{-2}$ | $R_{ct}/\Omega\cdot cm^2$ | $\tau_1/s$ | $\chi^2$ |
|---|---|---|---|---|---|---|---|
| ZrN | 12.64±0.05 | $(2.90\pm0.25)\times10^{-6}$ | 0.95±0.02 | 1.69 | $(1.06\pm0.07)\times10^{3}$ | 0.0018 | $2.49\times10^{-3}$ |
| - | - | $C_{coat}/\Omega^{-1}\cdot S^n\cdot cm^{-2}$ | $n_2$ | $C_b/\mu F\cdot cm^{-2}$ | $R_{coat}/\Omega\cdot cm^2$ | $\tau_2/s$ | - |
| - | - | $(9.07\pm0.08)\times10^{-7}$ | 0.92±0.02 | 0.34 | $(3.29\pm0.10)\times10^{7}$ | 11.19 | - |
| - | $R_s/\Omega\cdot cm^2$ | $Q_p/\Omega^{-1}\cdot S^n\cdot cm^{-2}$ | $n$ | $C_p/\mu F\cdot cm^{-2}$ | $R_p/\Omega\cdot cm^2$ | $\tau/s$ | $\chi^2$ |
| 316SS | 12.17±0.03 | $(1.09\pm0.06)\times10^{-5}$ | 0.91±0.03 | 4.51 | $(2.15\pm0.02)\times10^{5}$ | 0.97 | $1.35\times10^{-3}$ |